



**HAL**  
open science

## Microstructure, Critical Behavior and Magnetocaloric Properties of Melt-Spun Ni<sub>51.82</sub>Mn<sub>32.37</sub>In<sub>15.81</sub>

Karima Dadda, Safia Alleg, Saida Souilah, Jason Daza, Joan Saurina, Joan-Josep Suñol, Lotfi Bessais, El-Kebir Hlil

► **To cite this version:**

Karima Dadda, Safia Alleg, Saida Souilah, Jason Daza, Joan Saurina, et al.. Microstructure, Critical Behavior and Magnetocaloric Properties of Melt-Spun Ni<sub>51.82</sub>Mn<sub>32.37</sub>In<sub>15.81</sub>. *Magnetochemistry*, 2022, 8 (12), pp.179. 10.3390/magnetochemistry8120179 . hal-03983753

**HAL Id: hal-03983753**

**<https://hal.science/hal-03983753>**




Submitted on 16 Feb 2024

**HAL** is a multi-disciplinary open access archive for the deposit and dissemination of scientific research documents, whether they are published or not. The documents may come from teaching and research institutions in France or abroad, or from public or private research centers.

L'archive ouverte pluridisciplinaire **HAL**, est destinée au dépôt et à la diffusion de documents scientifiques de niveau recherche, publiés ou non, émanant des établissements d'enseignement et de recherche français ou étrangers, des laboratoires publics ou privés.

Article

# Microstructure, Critical Behavior and Magnetocaloric Properties of Melt-Spun Ni<sub>51.82</sub>Mn<sub>32.37</sub>In<sub>15.81</sub>

Karima Dadda<sup>1,2</sup>, Safia Alleg<sup>1,\*</sup>, Saida Souilah<sup>1,3</sup>, Jason Daza<sup>2</sup> , Joan Saurina<sup>2</sup>, Joan-Josep Suñol<sup>2,\*</sup> , Lotfi Bessais<sup>4</sup>  and El-Kebir Hlil<sup>5</sup>

<sup>1</sup> LM2S, Department of Physics, Université Badji Mokhtar Annaba, B.P. 12, Annaba 23000, Algeria

<sup>2</sup> Department of Physics, University of Girona, Campus Montilivi s/n, 17003 Girona, Spain

<sup>3</sup> ESTI Annaba, B.P. 218, Annaba 23000, Algeria

<sup>4</sup> CNRS-UPEC, Université Paris Est, ICMPE (UMR 7182), F-94320 Thiais, France

<sup>5</sup> Institut Néel, CNRS, Université Grenoble Alpes, 25 Rue des Martyrs, B.P. 166, CEDEX 9, F-18042 Grenoble, France

\* Correspondence: safia.alleg@univ-annaba.dz (S.A.); joanjosep.sunyol@udg.edu (J.-J.S.)

**Abstract:** Heusler alloy with an atomic composition of Ni<sub>51.82</sub>Mn<sub>32.37</sub>In<sub>15.81</sub> was prepared by melt spinning from arc-melted ingots. X-ray diffraction, scanning electron microscopy and magnetic measurements were used to study the structural, microstructural and magnetic properties. The crystal structure consists of a mixture of B2 austenite (~50%) and 14M martensite (~50%). The alloy undergoes a second order magnetic transition at a Curie temperature of  $T_c^A = 194.2$  K. The hysteresis loop reveals the occurrence of exchange bias phenomenon at room temperature. The critical exponents  $\beta$ ,  $\gamma$  and  $\delta$  were estimated using modified Arrott plots, Kouvel–Fisher curves and critical isothermal analysis. The respective values are  $\beta = 0.500 \pm 0.015$ ,  $\gamma = 1.282 \pm 0.055$  and  $\delta = 3.003 \pm 0.002$ . The critical behaviour in ribbons is governed by the mean field model with a dominated long-range order of ferromagnetic interactions. The maximum entropy change,  $\Delta S_M^{max}$ , for an applied magnetic field of 5 T reaches an absolute value of 0.92 J/kg·K. The experimental results of entropy changes are in good agreement with those calculated using Landau theory.

**Keywords:** Ni-Mn-In ribbons; magnetic transition; critical behavior; magnetocaloric effect; Landau theory



**Citation:** Dadda, K.; Alleg, S.; Souilah, S.; Daza, J.; Saurina, J.; Suñol, J.-J.; Bessais, L.; Hlil, E.-K.

Microstructure, Critical Behavior and Magnetocaloric Properties of Melt-Spun Ni<sub>51.82</sub>Mn<sub>32.37</sub>In<sub>15.81</sub>. *Magnetochemistry* **2022**, *8*, 179. <https://doi.org/10.3390/magnetochemistry8120179>

Academic Editor: Mingfang Qian

Received: 21 October 2022

Accepted: 28 November 2022

Published: 2 December 2022

**Publisher's Note:** MDPI stays neutral with regard to jurisdictional claims in published maps and institutional affiliations.



**Copyright:** © 2022 by the authors. Licensee MDPI, Basel, Switzerland. This article is an open access article distributed under the terms and conditions of the Creative Commons Attribution (CC BY) license (<https://creativecommons.org/licenses/by/4.0/>).

## 1. Introduction

Since structural and magnetic transformations have been reported in Ni-Mn-Z (Z = Ga, Sn, In) alloys [1], many studies on austenitic and martensitic states have been investigated [2–9]. Upon cooling, these alloys undergo a first order martensitic transition from a high temperature cubic austenite phase (Ast), displaying long ferromagnetic (FM) order, to a low temperature modulated or non-modulated martensite phase (Mst) with complex magnetic behavior. The magnetization is smaller in the Mst phase than in the Ast. Additionally, the magnetic coupling is FM in the high temperature phase and is short range antiferromagnetic (AFM) for Mn-rich compounds [10,11]. Moreover, the magnetic properties are dominated by Mn-Mn coupling in stoichiometric compositions of Ni<sub>2</sub>MnZ. However, FM – AFM interactions were found in off-stoichiometric alloys, in which Mn atoms occupying Z sites coupled antiferromagnetically to Mn atoms in their own regular sites.

Due to their good magneto-functional performances, these magnetic materials have attracted much attention owing to their potential application in magnetic refrigeration, spintronics and actuation [12,13]. These technological applications are related to the strong correlation between the magnetism and the structural transition such as the magnetocaloric effect (MCE), magnetostructural resistance, shape memory, exchange bias behaviour (EB), etc. [7,14–21]. Thus, any change in the chemical composition, sample preparation, type of

crystal structure homogeneity, heat treatment, application of an external magnetic field or stress can affect the phase transitions. MCE is strongly dependent on the type of magnetic transition. For example, most Heusler alloys have a second-order magnetic transition (SOMT), from FM to paramagnetic state (PM) around the Curie temperature ( $T_c$ ), resulting in a negative magnetic entropy change known as direct MCE, and a first-order magnetic transition resulting in a positive magnetic entropy change, known as inverse magnetocaloric effect (IMCE) near the martensitic transition [22,23].

Many studies have been conducted on polycrystalline Ni–Mn–In ingots prepared by arc melting and succeeding heat treatment at high temperature for homogenization. The crystal structure and physical properties can be affected considerably by a small change in composition and/or sample preparation as the magnetic interactions and their strength can be modified by the substitution of Mn atoms for Ni and In atoms. For example, a mixture of austenite and martensite phases was observed in bulk  $\text{Ni}_{50}\text{Mn}_{50-x}\text{In}_x$  ( $x = 14.8, 15.05$  and  $15.2$ ), while a single austenite phase (space group  $Fm\bar{3}m$ ) was observed for  $x = 14.5$ , and an orthorhombic martensite (space group  $Pmm2$ ) for  $x = 15$  [24]. In addition, the crystal structure of the arc-melted  $\text{Ni}_{50}\text{Mn}_{35}\text{In}_{15}$  consisted of a mixture of austenite and orthorhombic martensite having different magnetic transition temperatures of about  $T_c^A = 310$  K and  $T_c^M = 200$  K, respectively. For the as-quenched  $\text{Ni}_{51.1}\text{Mn}_{31.2}\text{In}_{17.7}$ , the disordered  $B2$  structure, which is observed at room temperature, transformed into an ordered  $L2_1$  structure after a short annealing time [25]. It is important to mention that the arc melting process may cause different problems that negatively affect the functional properties of the alloys [26]. Hence, the melt-spinning process can be considered as an alternative way of produce ribbons in a metastable state with homogeneous chemical composition avoiding annealing at high temperature [27]. Furthermore, it is possible to obtain a nearly single-phase [8,28] and highly textured microstructure owing to the high cooling rate ( $\sim 10^6$  K/s), which leads to a change in the atomic order. Consequently, this fact is of great interest to investigate. Additionally, the ribbon's shape could be used mainly as sensors and actuators, and in magnetocaloric devices.

The current work was carried out to investigate the effect of the melt-spinning process on the structure, morphology and magnetic properties of melt-spun  $\text{Ni}_{50}\text{Mn}_{35}\text{In}_{15}$  ribbons. Structure, morphology and magnetic properties were studied using X-ray diffraction, scanning electron microscopy (SEM) coupled with energy-dispersive X-ray spectroscopy (EDS), and magnetic measurements. In order to distinguish the nature of the magnetic interaction around the magnetic transition, the critical behavior around the Curie temperature was investigated through isothermal magnetization data,  $M(H)$ , using several techniques [29] of the conventional critical exponents for the mean field model (MF)  $\beta = 0.5$  and  $\gamma = 1$ , 3D Heisenberg model  $\beta = 0.365$  and  $\gamma = 1.336$ , 3D Ising model  $\beta = 0.325$  and  $\gamma = 1.241$ , and for tricritical mean field model  $\beta = 0.25$  and  $\gamma = 1$ . Thus, the Curie temperature and the critical exponents were estimated.

## 2. Materials and Methods

Polycrystalline ribbons with nominal composition of  $\text{Ni}_{51.82}\text{Mn}_{32.37}\text{In}_{15.81}$  were prepared by melt-spinning at high wheel speed of 40 m/s from arc-melted pure elements. An ingot of about 5 g was prepared from high purity (>99.98%) Ni, Mn and In elements (Sigma Aldrich, Saint Louis, MO, USA) by arc melting in a MAM-1 Buhler (Edmund Bühler GmbH, Bodelshausen, Germany) compact arc melter, in a water-cooled copper crucible, under argon atmosphere. The ingot was melted several times to ensure good homogeneity. The ribbons were obtained in a MSP10 melt-spinning system (Edmund Bühler GmbH, Bodelshausen, Germany), under argon atmosphere (400 mbar), onto a polished surface of copper wheel rotating at a linear speed of 40 m/s, with a nozzle wheel distance of 3 mm, an orifice diameter of 0.5 mm and an injection pressure of 500 mbar.

Magnetization measurements versus temperature were carried out using BS1 magnetometer developed at Néel Institute. The hysteresis loop, at room temperature, was measured with a Lake Shore 7400 VSM vibrating sample magnetometer (Lake Shore Cryotronics,

Westerwille, OH, USA). Ribbons' morphology was investigated using a scanning electron microscope (SEM, TESCAN, Brno, Czech Republic) operating at 30 kV and equipped with the energy dispersive X-ray spectrometer (EDS, TESCAN, Brno, Czech Republic). The alloy structure was followed by X-ray diffraction (XRD) on a D8 Advance diffractometer (Bruker, Billerica, MA, USA) in a  $(\theta-2\theta)$  Bragg Brentano geometry using Cu-K $\alpha$  radiation ( $\lambda_{\text{Cu}} = 0.154056$  nm). The XRD analysis was carried out using the Maud program [30], which is based on the Rietveld method.

### 3. Results and Discussion

#### 3.1. Structure and Morphology

Figure 1 displays secondary electron SEM micrographs showing the fracture cross section microstructure, wheel surface microstructure and free surface microstructure of Ni<sub>51.82</sub>Mn<sub>32.37</sub>In<sub>15.81</sub> as-spun ribbons. One observes that the grains are highly ordered columnar-like microstructures with their longer axis being perpendicular to the ribbon sides (Figure 1c). The wheel surface shows typical elongated thin plates corresponding to martensite variants (Figure 1a), and the free surface displays granular microstructure with different grain sizes and shapes (Figure 1b). EDS element-mapping over one defined region indicates that the three elements (Ni, Mn, and In) are homogeneously distributed (Figure 1d). From EDS analysis over many points an average elemental composition Ni<sub>51.82</sub>Mn<sub>32.37</sub>In<sub>15.81</sub> is obtained. Therefore, the electron-to-atom ratio ( $e/a$ ) calculated from the outer shell of each element is 7.922.

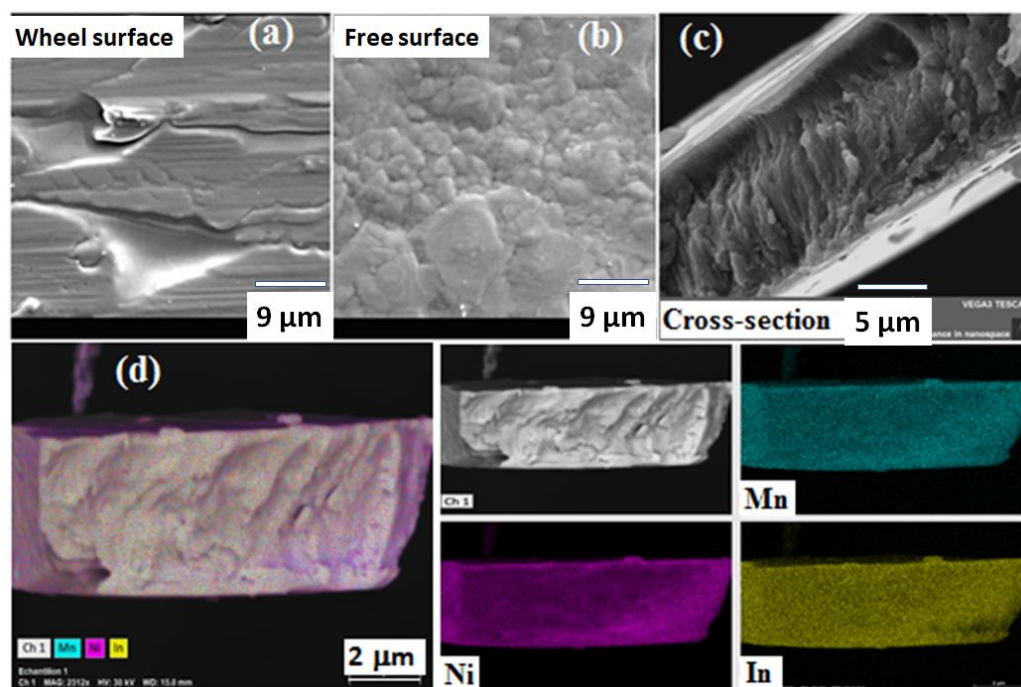


**Figure 1.** Typical SEM micrographs of wheel surface (a), free surface (b), fracture cross-section (c), and (d) EDS element-mapping of Ni<sub>51.82</sub>Mn<sub>32.37</sub>In<sub>15.81</sub> ribbons.

Rietveld refinement of the XRD pattern of the melt-spun ribbons (Figure 2) reveals the coexistence of a seven-layered monoclinic 14M structure,  $P2/m$  space group, with lattice parameters  $a = (4.3381 \pm 0.0002)\text{\AA}$ ,  $b = (5.5642 \pm 0.0002)\text{\AA}$  and  $c = (29.235 \pm 0.0005)\text{\AA}$  and  $\beta = 92.92^\circ$ , and a cubic B2 austenite structure, space group  $Pm\bar{3}m$ , and a lattice parameter of  $a = (2.9684 \pm 0.0002)\text{\AA}$ . The relative deviations of the lattice parameters shown by:  $\Delta a = \frac{(a-a_0)}{a_0}$ ,  $\Delta b = \frac{(b-b_0)}{b_0}$ , and  $\Delta c = \frac{(c-c_0)}{c_0}$  where  $a_0$ ,  $b_0$  and  $c_0$  are the lattice parameters of a perfect crystal, reaching as much as  $\Delta a = 0.88\%$ ,  $\Delta b = -3.6\%$  and  $\Delta c = 0.81\%$  for the 14M structure, and  $\Delta a = -1.6\%$  for the B2 austenite. In addition, the weight fractions of both the 14M martensite and B2 austenite structures are equal to 50%, and their

crystallite sizes are of about 65 nm and 96 nm, respectively. The nanocrystalline state of the obtained ribbons can be attributed to the atomic disorder, which is induced by the rapid solidification of the melt-spun ribbons.

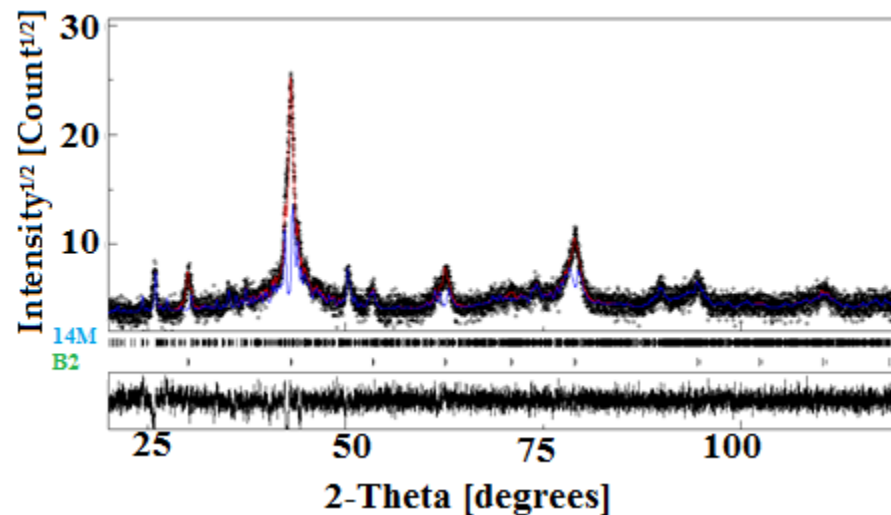
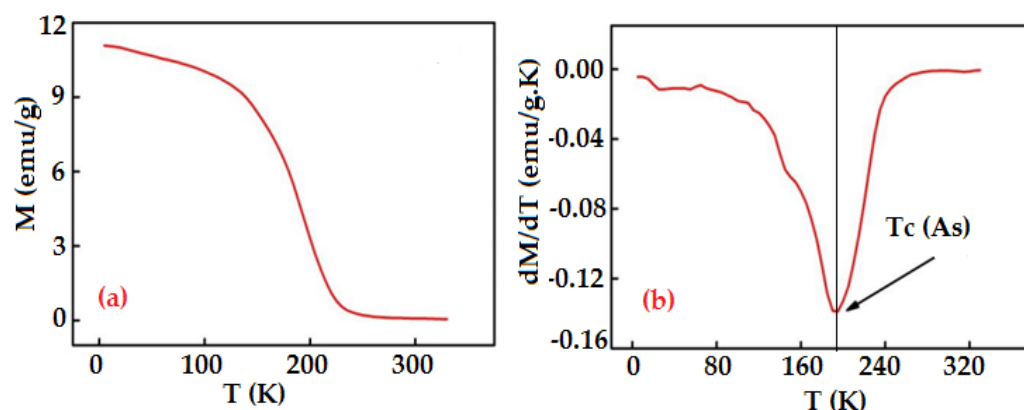


Figure 2. Rietveld refinement of the XRD pattern of melt-spun ribbons.

Krenke et al. reported that bulk  $\text{Ni}_{0.5}\text{Mn}_{0.5-x}\text{In}_x$  ( $x = 0.05 - 0.25$ ) alloys displayed an austenite structure with  $x$  ranging from 0.16 to 0.25, and a martensite structure for  $0.05 \leq x \leq 0.155$  [2]. Çakir et al. reported that bulk  $\text{Ni}_{50}\text{Mn}_{50-x}\text{In}_x$  exhibited modulated 7M and austenite structures for  $x = 14.4$  [31]. Sánchez Llamazares et al. found that  $\text{Ni}_{51.1}\text{Mn}_{31.2}\text{In}_{17.7}$  ribbons presented a B2 structure [25]. The obtained result differs from those reported above, since the elaboration technics affect the alloy composition and physical properties. Furthermore, the martensitic transformation temperature can be twined by electron-to-atom ratio, Mn nearest neighbor interatomic distances, atomic order degree and crystallite size [32,33]. From differential calorimetry scans (not shown here), no structural transformation was detected in these ribbons since the modulated martensite has a lower symmetry than the austenite, and the B2 structure is considered as disordered compared to the  $L2_1$  structure. Such structural complexity can affect other physical properties, especially the magnetic results.

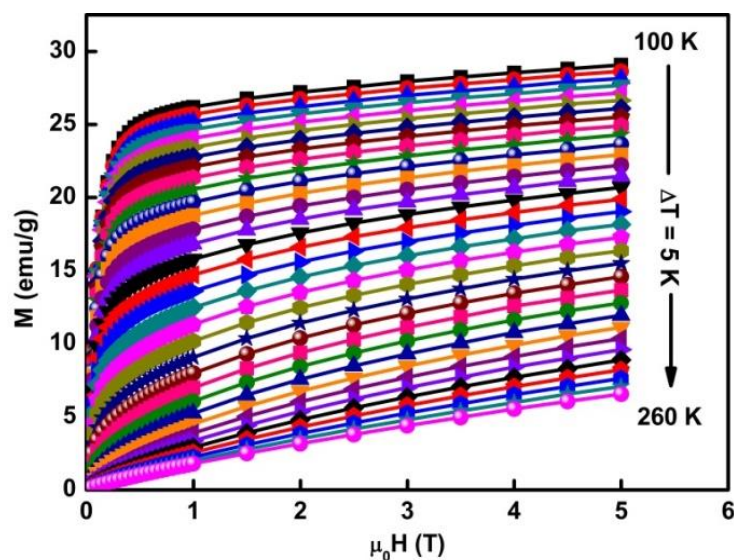
### 3.2. Magnetic Properties

Figure 3a displays magnetization evolution versus temperature  $M(T)$ , in the temperature range 5–330 K, upon cooling under an applied magnetic field of 500 Oe. The melt-spun ribbons exhibit a paramagnetic to ferromagnetic transition at the Curie temperature of austenite,  $T_c(A_s) = 194.2$  K, which is defined as the minimum peak position of  $dM/dT$  curve (Figure 3b).



**Figure 3.** Temperature dependence of the magnetization measured at 500 Oe (a), and the derivative  $dM/dT$  curve showing the magnetic transition temperature ( $T_c$  (As)) (b).

The isothermal magnetization curves as a function of the applied magnetic field,  $M(H)$ , are shown in Figure 4. All the curves do not saturate even at 5 T and show a typical FM character when  $T < 194.2$  K and PM behavior when  $T > 194.2$  K. According to Banerjee's criteria [34], the second order FM – PM phase transition (SOMT) is characterised by a positive slope in Arrott curves,  $M^2$  versus  $\mu_0 H/M$ . Thus, the studied ribbons undergo SOMT phase transition since they show a positive slope (Figure 5). In the low-field region,  $M^2 = f(\mu_0 H/M)$  curves have two parts in the opposite directions indicating the FM – PM separation. However, in the vicinity of  $T_c$ , a linear  $M^2 = f(\mu_0 H/M)$  line passing through the coordinate origin is observed. Hence, the  $T_c$  value deduced from the Arrott plots is very close to that obtained from  $M(T)$ . This feature supports evidence of the long-rang FM-order character of the sample.



**Figure 4.** Isothermal magnetization around  $T_c^A$  at different temperatures from 100 to 260 K (increments of 5 K).

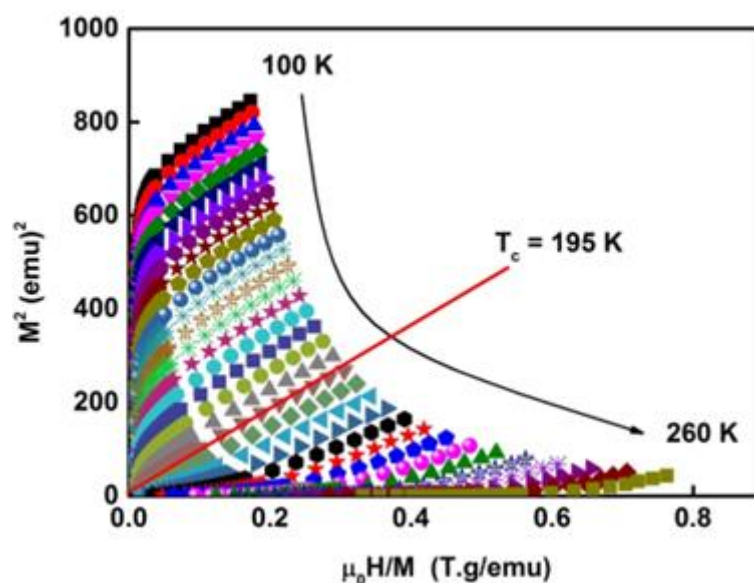


**Figure 5.** Standard Arrott plot isotherms  $M^2$  vs.  $\mu_0 H/M$ . From 100 to 260 K (increments of 5 K).

Figure 6 displays the enlargement of the low magnetic field region of the hysteresis loop measured, at room temperature, under an applied magnetic field of 2 T. The inset shows the hysteresis cycle. This later exhibits a nearly straight line typical of a paramagnetic-type compartment due to the increase of atomic disorder, which is a characteristic of the melt-spinning process. Furthermore, the hysteresis loop shows a positive horizontal shift and a negative vertical shift. The horizontal H-axis shift can be related to the development of a magnetically non-homogeneous AF/FM matrix where the interfacial pinning of FM spins by the AF component gives rise to an exchange bias (EB) behavior at room temperature. The exchange bias phenomenon is associated with the exchange anisotropy created at the interface between AFM and FM regions and can be ascribed to the formation of an FM unidirectional anisotropy (texture) at the interface between different magnetic phases during the formation of the ribbons. This result is different from those reported earlier for a similar composition where the EB was observed at lower temperature of martensitic state in bulk  $\text{Ni}_{50}\text{Mn}_{35}\text{In}_{15}$  alloy [31]. The obtained result confirms the fact that the processing conditions, crystal structure and microstructure affect considerably the magnetic properties leading to the observation of EB in the  $\text{Ni}_{51.82}\text{Mn}_{32.37}\text{In}_{15.81}$  ribbons at room temperature. The values of EB and the coercivity field are calculated using  $H_E = -(H_1 + H_2)/2$  and  $H_c = |H_1 - H_2|/2$ , respectively, where  $H_1$  and  $H_2$  are the left and the right field values at zero magnetization. Hence, the coercivity and EB values are 48.54 Oe and 100 Oe, respectively.

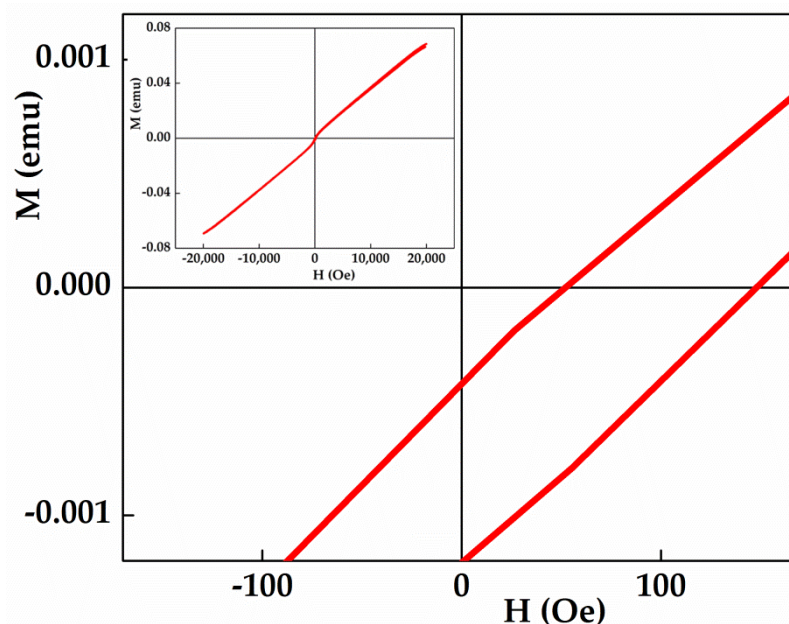


**Figure 6.** Enlargement of the low magnetic field region of the hysteresis loop measured at room temperature. The inset shows the corresponding hysteresis cycle.

The vertical shift observed in the magnetization curve may be attributed to the strong AFM interactions in the martensite structure and/or to the short-range AFM magnetic coupling in the Mn-rich areas. Indeed, the rapid solidification leads to structural heterogeneities owing to the temperature difference between the free and wheel surfaces of the ribbons. It is obvious that a small change in the composition or in the elaboration conditions affects the physical properties of the Heusler alloys as shown in Table 1 [2,35,36].

**Table 1.** Comparison of the obtained physical properties of  $\text{Ni}_{51.82}\text{Mn}_{32.37}\text{In}_{15.81}$  ribbons with earlier reports.

| Sample  | Method                                       | $ea$  | Phase                        | $a, b, c$ (Å)  | $T_c$ (K) | $\pm\Delta S$ (J/kg.K) | $H_c$ (Oe)  | Ref.      |
|---|--|-------|------------------------------|--|-----------|------------------------|-------------|-----------|
| $\text{Ni}_{51.82}\text{Mn}_{32.37}\text{In}_{15.81}$ | Melt spinning                                | 7.922 | cubic $B2$<br>$14 M$         | $a = 2.968$<br>$a = 4.327$<br>$b = 5.567$<br>$c = 29.035$  | 194.2     | 0.92 (5 T)             | 48.54 (2 T) | This work |
| $\text{Ni}_{50}\text{Mn}_{35}\text{In}_{15}$          | Arc melting and annealing at 1073 K for 2 h  | 7.902 | $10 M$                       | $a = 4.391$<br>$b = 5.882$<br>$c = 21.184$                 |           |                        |             | [2]       |
| $\text{Ni}_{51}\text{Mn}_{33.4}\text{In}_{15.6}$      | Arc melting and annealing at 1173 K for 48 h |       | cubic $L2_1$                 | $a = 6.008$  | 309.5     | 15 (5 T)               |             | [35]      |
| $\text{Ni}_{52}\text{Mn}_{32.5}\text{In}_{15.5}$      | Arc melting and annealing at 1173K for 48 h  |       | cubic $L2_1$<br>orthorhombic | $a = 6.010$<br>$a = 17.961$<br>$b = 10.766$<br>$c = 4.608$ | 182       |                        |             | [31]      |

### 3.3. Critical Behavior

The critical exponents  $\beta$ ,  $\gamma$  and  $\delta$  characterize the samples that underwent SOMET. The exponent  $\beta$ , which is linked to the evolution of the spontaneous magnetization with respect to the temperature ( $M_s \propto (T - T_c)^\beta$ ), describes the growth of the ordered moment below  $T_c$ ;  $\gamma$  is related to the temperature dependence of the initial magnetic susceptibility ( $\chi_0^{-1} \propto (T - T_c)^\gamma$ ). It defines the divergence of  $\chi_0$  at  $T_c$ , and  $\delta$  is associated with the critical isothermal magnetization. It describes the curvature of the isothermal magnetization curves  $M(H)$  at  $T_c$ . For further confirmation of the long-range nature of FM interactions that



characterize the sample, the modified Arrott plots (MAPs) [37] are presented for the mean field model, 3D-Heisenberg model, 3D-Ising model and tricritical mean field model in Figure 7.

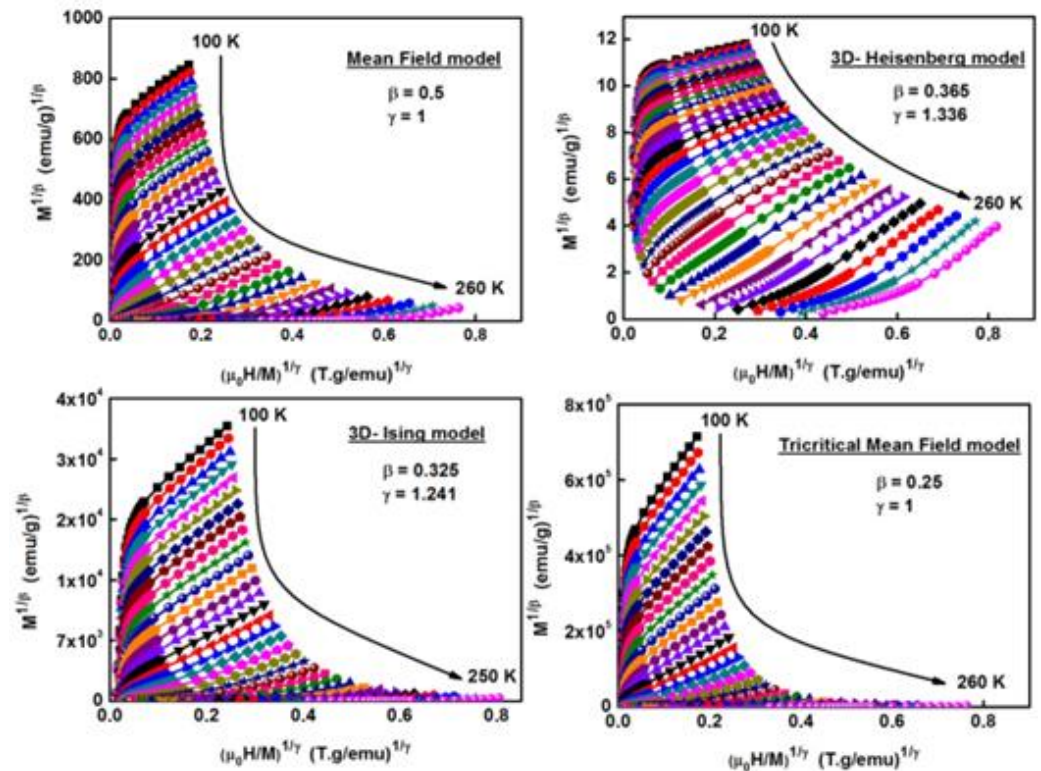


**Figure 7.** Modified Arrott plots: isotherms of  $M^{1/\beta}$  vs.  $(H/M)^{1/\gamma}$  with the mean field model, 3D-Heisenberg model, 3D-Ising model and tricritical mean field model. From 100 to 260 K (increments of 5 K).

These models are used to plot the calculated relative slope  $RS$  using the linear fit from the high field region of each curve. The relative slope, which is given by  $RS = S(T)/S(T_{Cr})$  (Figure 8), is identified as the ratio between the slope at each temperature,  $S(T)$ , and the slope at the critical temperature,  $S(T_{Cr})$ . Generally, for a given conventional model,  $RS$  is much closer to the unit. Accordingly, the critical behaviour of the ribbons can be well-described by the mean field, MF, with a dominated long-range order of ferromagnetic interactions. Similar critical behaviour was reported for the  $\text{Ni}_{43}\text{Mn}_{46}\text{Sn}_8\text{In}_3$  Heusler alloy prepared by arc melting and annealing at 1323 K for 48 h. The small deviations in critical exponents  $\beta$  and  $\gamma$  from those expected for the mean field model were related to the coexistence of FM and AFM interactions in the alloy [38]. It is obvious that preparation conditions and, consequently, the alloy's microstructure influences their critical behavior considerably.

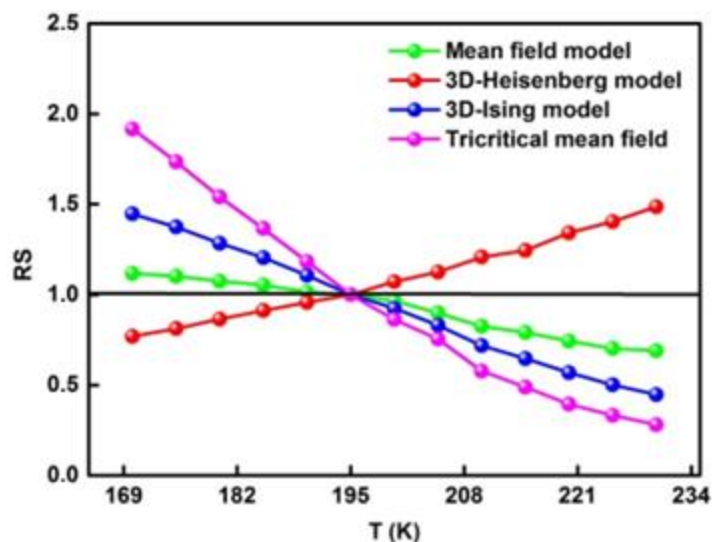


**Figure 8.** Relative slope (RS) as function of temperature defined as  $RS = S(T)/S(T_{cr})$  using different models.

The first estimation of  $\beta$  and  $\gamma$  values as well as  $T_c$  are provided through the non-linear fit of the spontaneous magnetization  $M_s(T, 0)$  and the inverse of the initial susceptibility  $\chi_0^{-1}(T, 0)$  curves using Equations (1) and (2), respectively:

$$M_S(T) = M_0(-\varepsilon)^\beta; \varepsilon < 0, \quad T < T_c \tag{1}$$

$$\chi_0^{-1}(T) = \left(\frac{h_0}{M_0}\right)\varepsilon^\gamma; \varepsilon > 0, \quad T > T_c \tag{2}$$

$$M = DH^{1/\delta}; \varepsilon = 0, \quad T = T_c \tag{3}$$

where  $\varepsilon = (T - T_c)/T_c$  is the reduced temperature,  $M_0$ ,  $h_0$  and  $D$  are the critical amplitudes. The values of  $\beta$ ,  $\gamma$  and  $T_c$  are shown in Figure 9, in which  $\beta = 0.500 \pm 0.015$ ,  $\gamma = 1.282 \pm 0.055$  and  $T_c = (198.456 \pm 1.077)$  K are close to the MF model and the estimated  $T_c$  is closer to the obtained value from the  $M(T)$  curve.

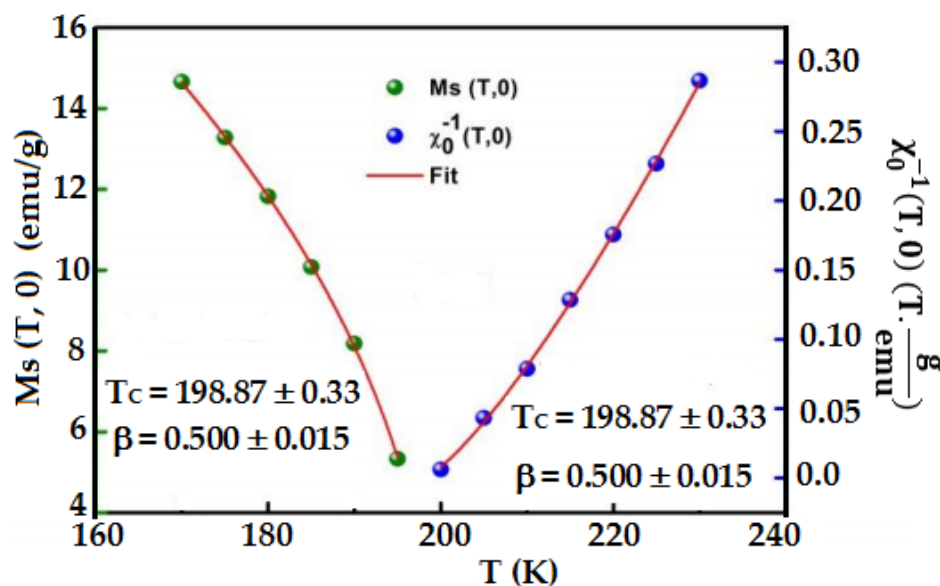


**Figure 9.** Temperature dependence of spontaneous magnetization  $M_S(T, 0)$  and the inverse of initial susceptibility  $\chi_0^{-1}(T, 0)$ .

Straight-lined Kouvel–Fisher plots [39,40] ( $K - F$ ) of  $M_S(T)(dM_S(T)/dT)^{-1}$  and  $\chi_0^{-1}(T)(d\chi_0^{-1}(T)/dT)^{-1}$  vs.  $T$ , with slopes  $1/\beta$  and  $1/\gamma$ , show the most precise values of the critical exponents and  $T_c$ . This was later determined by an extrapolation to the T-axis (Figure 10). One observes that the accurate values are close to those obtained from the MAPs. The value of the third exponent  $\delta$  can be determined directly from the critical isotherm (CI) curve  $M = f(\mu_0 H, T_c)$  (Figure 11). The inset in Figure 11 displays the log–log plot, where the linear fit using Equation (3) leads to a value of  $\delta = 3.003 \pm 0.002$ . The accuracy of the gained exponent values  $\beta$  and  $\gamma$  are interrelated to the third exponent  $\delta$  via Widom scaling relation ( $\delta = 1 + (\gamma/\beta)$ ) [41]. The calculated  $\delta = 3.353 \pm 0.027$  is slightly large than that determined experimentally from the critical isotherm  $\delta = 3.003 \pm 0.002$ . The difference may be attributed to the coexistence of  $14M$  and  $B2$  structures leading to the coexistence of FM and AFM interactions in the prepared Heusler alloy. Consequently, the temperature dependence of the initial magnetic susceptibility can be affected. Critical exponents often show a deviation from the values of theoretical models. This appears as if a magnetic system is governed by various competing coupling and/or disorders [42,43].

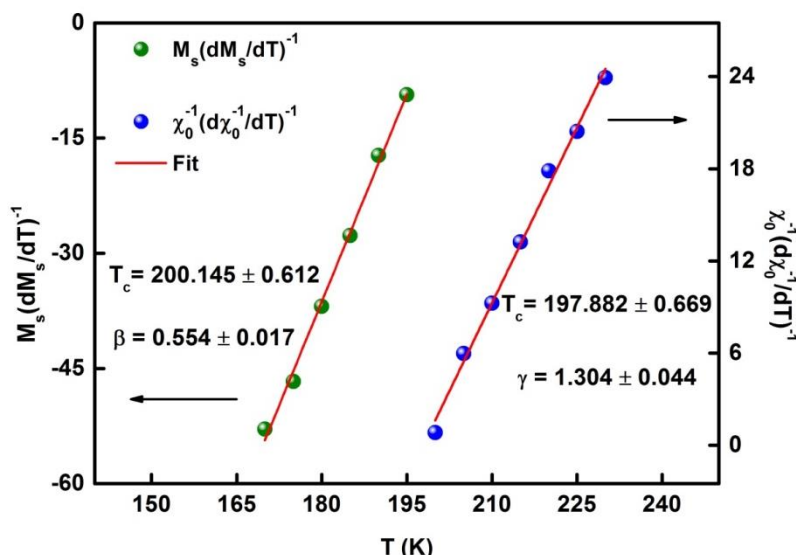


Figure 10. Kouvel–Fisher plots for the spontaneous magnetization and the inverse of initial susceptibility.

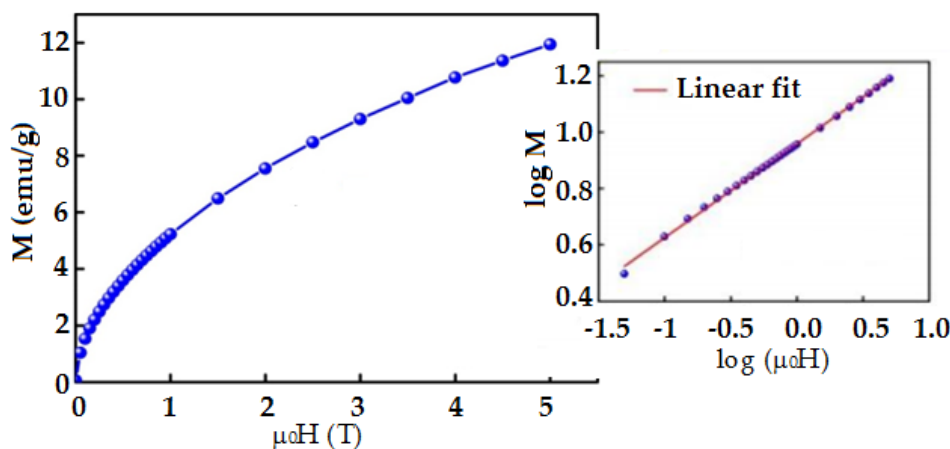
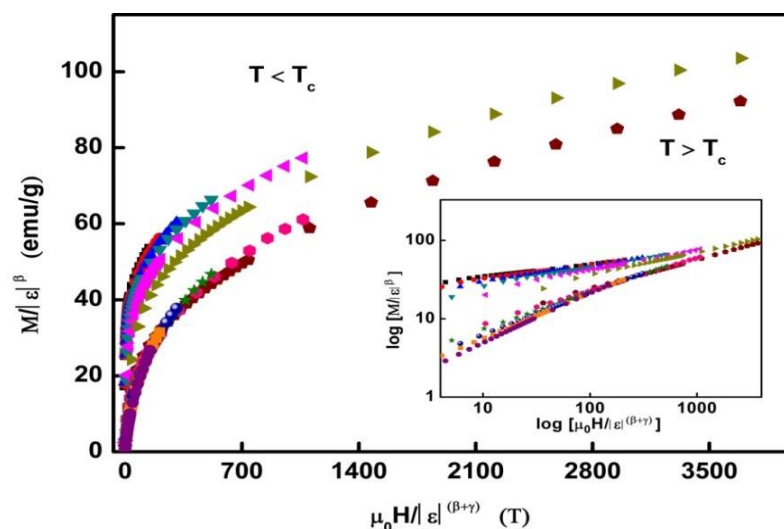


Figure 11. Critical isotherms of  $M(\mu_0 H, T_c^A)$ . The inset shows the logarithmic scale.

The reliability of the obtained critical exponents and  $T_c$  values can be confirmed by the scaling hypothesis [44], which presents two distinct branches below and above  $T_c$ ;

confirming that the estimated critical exponents and  $T_c$  are reasonably accurate (Figure 12). As summarized in Table 2, the estimated values match well the mean field model [29,30,45].



**Figure 12.** Scaling plots (following the procedure described in ref. [28] where the points correspond to regular analytical functions) indicating universal curves above and below  $T_c^A$ . The inset shows the same plot in log–log scale.

**Table 2.** Comparison of estimated critical exponents of  $\text{Ni}_{51.82}\text{Mn}_{32.37}\text{In}_{15.81}$  ribbons with other reports and the various theoretical models.

| Material  | Technique | $\beta$           | $\gamma$          | $\delta$          | Ref.      |
|---|-----------|-------------------|-------------------|-------------------|-----------|
| $\text{Ni}_{51.82}\text{Mn}_{32.37}\text{In}_{15.81}$   | MAPs      | $0.500 \pm 0.015$ | $1.282 \pm 0.055$ | —                 | This work |
|   | K-F       | $0.554 \pm 0.017$ | $1.304 \pm 0.044$ | $3.353 \pm 0.027$ |           |
|   | CI        | —                 | —                 | $3.003 \pm 0.002$ |           |
| $\text{Ni}_{50}\text{Mn}_{35}\text{In}_{14}\text{Si}_1$ | MAPs      | 0.510             | 0.987             | 2.935             | [44]      |
|   | CI        | —                 | —                 | 2.950             |           |
|   | MAPs      | 0.550             | 0.944             | 2.716             |           |
| $\text{Ni}_{50}\text{Mn}_{35}\text{Sn}_{15}$            | CI        | —                 | —                 | 2.670             | [30]      |
|   | MAPs      | $0.50 \pm 0.03$   | $0.92 \pm 0.03$   | —                 |           |
|   | K-F       | $0.45 \pm 0.01$   | $0.88 \pm 0.03$   | 2.92              |           |
|   | CI        |                   |                   | $3.02 \pm 0.02$   |           |
| Mean field model  |           | 0.5               | 1.0               | 3.0               | [29]      |
| 3D Heisenberg model                                     |           | 0.365             | 1.336             | 4.80              | [29]      |
| 3D Ising model  |           | 0.325             | 1.241             | 4.82              | [29]      |
| Tricritical mean field                                  |           | 0.25              | 1.0               | 5.0               | [29]      |

### 3.4. Magnetocaloric Effect

The MCE can be evaluated by calculating the magnetic entropy change ( $\Delta S_M$ ). This is calculated by using the thermodynamic Maxwell relation as follows:

$$\Delta S_M(T, \Delta H) = S_M(T, H_2) - S_M(T, H_1) = \int_{H_1}^{H_2} \left( \frac{\partial M}{\partial T} \right)_T dH \quad (4)$$

where  $H_1$  and  $H_2$  are the applied fields and  $\Delta H = H_2 - H_1$ ,  $H_1 \leq H_2$ .

Numerically,  $\Delta S_M$  can be deduced by the integration of the magnetic isotherm plots at small discrete magnetic field and temperature intervals, and can be approximated as follows:

$$\Delta S_M(T, M) = \sum_i \frac{M_{i+1}(T_{i+1}, H_{i+1}) - M_i(T_i, H_i)}{T_{i+1} - T_i} \Delta H \quad (5)$$

where  $M_i$  and  $M_{i+1}$  are the experimental data of the magnetization at temperatures  $T_i$  and  $T_{i+1}$ , respectively, under a magnetic field  $H_i$ . Figure 13 displays the  $-\Delta S_M$  versus  $T$  plots for different applied magnetic fields ranging from 1 to 5 T. One observes that the magnetic entropy's peak ( $-\Delta S_M^{max}$ ) rises continuously with increasing the field from 0.11 to 0.92 J/kg.K for 1 T and 5 T, respectively (inset in Figure 13). This value is lower than that obtained for the melt-spun Ni<sub>50</sub>Mn<sub>35</sub>Sn<sub>15</sub> ribbons [28] and bulk Ni<sub>51</sub>Mn<sub>33.4</sub>In<sub>15.6</sub> alloy [35]. The much lower magnetic entropy change compared to that of the polycrystalline Ni<sub>51</sub>Mn<sub>33.4</sub>In<sub>15.6</sub> sample prepared by arc melting, followed by annealing at 1173 K for 48 h and quenching in ice water [35], can be associated with the modifications in the magnetic order of the sample, which is related to the preparation conditions and crystal structure. This later consists of a single cubic cell (space group  $Fm\bar{3}m$ , and  $a = 6.008(2) \text{ \AA}$ ) for the bulk Ni<sub>51</sub>Mn<sub>33.4</sub>In<sub>15.6</sub>, and a mixture of 14 M martensite (50%) and cubic B2 austenite structure (50%), (space group  $Pm\bar{3}m$ , and  $a = 2.9684 \text{ \AA}$ ) for the ribbons.

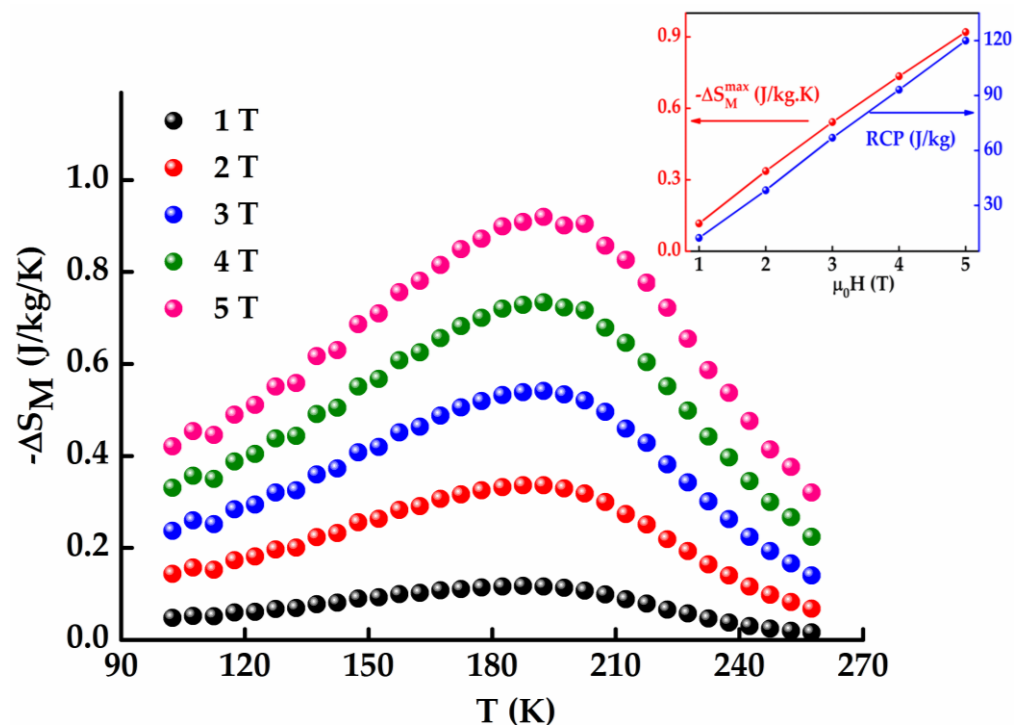


**Figure 13.**  $-\Delta S_M(T)$  curves for Ni<sub>51.82</sub>Mn<sub>32.37</sub>In<sub>15.81</sub> ribbons under applied fields of 1–5 T. The inset shows magnetic field dependence of  $-\Delta S_M^{max}$ .

The theoretical model proposed by Amaral et al. takes into account the contribution of the magneto-elastic electron's interactions [46]. The model is based on Landau theory in the vicinity of  $T_c$  [47]. In this model, free energy ( $G$ ) is developed as a function of magnetization ( $M$ ) as follows:

$$G(M, T) = G_0 + \frac{a(T)}{2} M^2 + \frac{b(T)}{4} M^4 + \frac{c(T)}{6} M^6 + \dots - HM \quad (6)$$

Considering the equilibrium condition,  $\partial G/\partial M = 0$ , the total magnetization around  $T_c$  can be described as follows:

$$H = a(T)M + b(T)M^3 + c(T)M^5 \quad (7)$$

By using Equation (7), the polynomial fit of the experimental  $M(H)$  data can be used to determine Landau's coefficient  $a(T)$ ,  $b(T)$  and  $c(T)$ . One notes that the  $a(T)$  value is always positive and presents a minimum around  $T_c$ , and the  $b(T)$  value can be negative, zero or positive. Additionally,  $b(T_c) = 0$  confirms that the transition belongs to the second order character. The  $c(T)$  value is always negative. Accordingly, the calculated values are in good agreement with the Landau model.

The magnetic entropy change can be modelled theoretically by using the derivative of the free energy with respect to the temperature according to the subsequent equation:

$$-\Delta S_M(T, H) = \left( \frac{dG}{dT} \right)_{\mu_0 H} = \frac{a'(T)}{2} M^2 + \frac{b'(T)}{4} M^4 + \frac{c'(T)}{6} M^6 \quad (8)$$

where  $a'(T)$ ,  $b'(T)$  and  $c'(T)$  are the derivative of Landau's coefficient with respect to temperature. The plots of the numeric calculation of  $-\Delta S_M$  are in good concordance with experimental results as illustrated in Figure 14. One observes that in the PM region ( $T > T_c$ ),  $(-\Delta S_M)_{exp}$  and  $(-\Delta S_M)_{theo}$  are well superposed, suggesting that the calculated Landau's coefficients are accurate. The small deviations around the maximum of the magnetic entropy curves can be related to the numerical derivatives that are introduced in the calculation, which may present a source of errors close to the transition temperature. In addition, these deviations may be attributed to the existence of inhomogeneous magnetism that could be associated with the coexistence of FM and AFM interactions in this Heusler alloy.

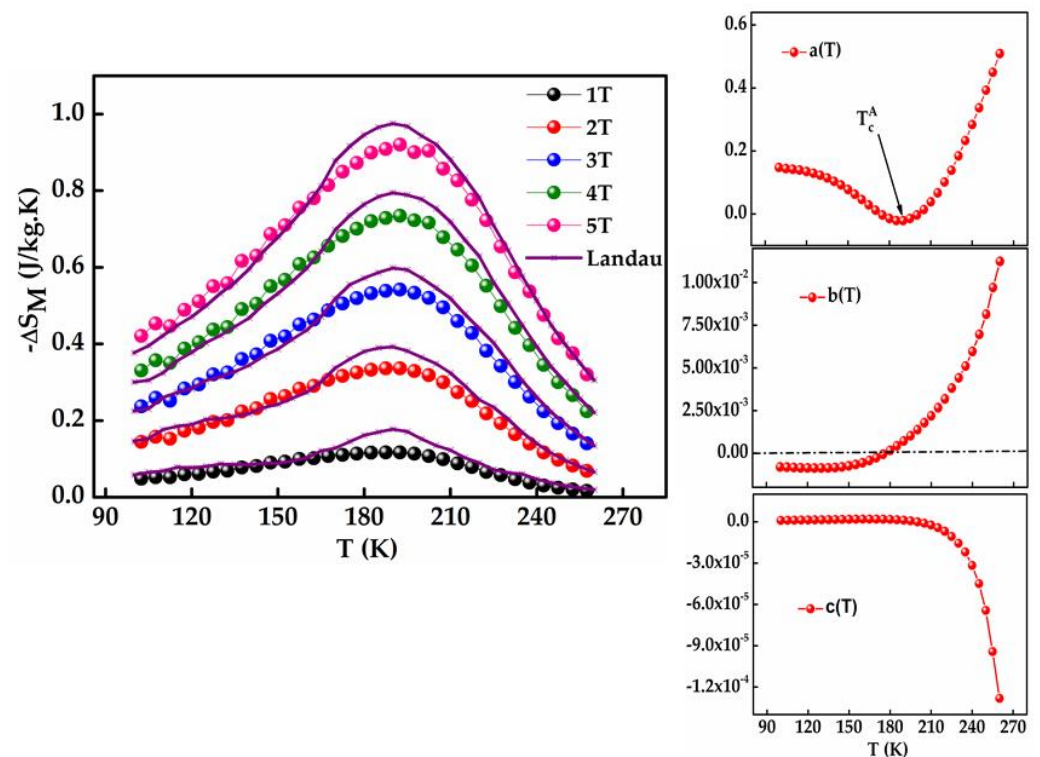


**Figure 14.** Superposition of experimental and calculated  $-\Delta S_M(T)$  curves for  $\text{Ni}_{51.82}\text{Mn}_{32.37}\text{In}_{15.81}$  ribbons under applied fields of 1–5 T (left), and the corresponding Landau coefficient  $a(T)$ ,  $b(T)$  and  $c(T)$  (right).

#### 4. Conclusions

Heusler  $\text{Ni}_{51.82}\text{Mn}_{32.37}\text{In}_{15.81}$  ribbons were prepared by melt-spinning from arc-melted ingots. The crystal structure consisted of a mixture of B2 austenite (~50%) and 14M martensite (~50%). The SOMT occurred at a Curie temperature of  $T_C^A = 194.2$  K. The occurrence of the exchange bias, at room temperature, can be related to the experimental conditions. The exchange bias can be ascribed to the coupling of AFM and FM at the interfaces. According to the critical exponent values ( $\beta = 0.500 \pm 0.015$ ,  $\gamma = 1.282 \pm 0.055$  and  $\delta = 3.003 \pm 0.002$ ), the critical behavior is governed by the mean field model with a dominated long-range order of ferromagnetic interactions. The maximum entropy change reached an absolute value of 0.92 J/kg·K for an applied magnetic field of 5 T. The experimental results from the magnetic entropy changes are in good agreement with those calculated using the Landau theory.

**Author Contributions:** Formal analysis: K.D., S.S. and E.-K.H.; supervision: S.A. and J.-J.S.; investigation: L.B., J.S. and E.-K.H.; writing—original draft preparation: S.A., J.D. and K.D. All authors have read and agreed to the published version of the manuscript.

**Funding:** This work has been supported by the DGRSDT/Algerian Ministère de l'Enseignement Supérieur et de la Recherche Scientifique, Spanish MINECO project MAT2016-75967-P and the Erasmus+k107 STA program.

**Institutional Review Board Statement:** Not applicable.

**Informed Consent Statement:** Not applicable.

**Data Availability Statement:** Data can be requested from the authors.

**Conflicts of Interest:** The authors declare no conflict of interest.

#### References

1. Sutou, Y.; Imano, N.; Koeda, N.; Omori, T.; Kainuma, R.; Ishida, K.; Oikawa, K. Magnetic and martensitic transformations of Ni-Mn-X (X = In, Sn, Sb) ferromagnetic shape memory alloys. *Appl. Phys. Lett.* **2004**, *85*, 4358–4360. [[CrossRef](#)]
2. Şaşmaz, M. Metamagnetic transition and magnetocaloric properties of  $\text{Ni}_{45}\text{Mn}_{42}\text{In}_{13}$  Heusler alloy. *Phase Transit.* **2021**, *94*, 289–297. [[CrossRef](#)]
3. Fan, J.L.; Zhao, G.M.; Ai, Y.L.; Ouyang, S.; Zhu, Y. Partially ordered hierarchical substructure of as cast? phase in Ni-Mn-Ga alloys. *Mater. Design* **2022**, *219*, 110780. [[CrossRef](#)]
4. Zhou, L.; Mehta, A.; Giri, A.; Cho, K.; Sohn, Y. Martensitic transformation and mechanical properties of  $\text{Ni}_{49+x}\text{Mn}_{36-x}\text{In}_{15}$  (x = 0, 0.5, 1.0, 1.5 and 2.0) Alloy. *Mater. Sci. Eng. A* **2015**, *646*, 57–65. [[CrossRef](#)]
5. Wederni, A.; Ipatov, M.; González, J.M.; Khitouni, M.; Suñol, J.J. Ni-Mn-Sn-Cu alloys after thermal cycling: Thermal and magnetic response. *Materials* **2021**, *14*, 6851. [[CrossRef](#)]
6. Dubiel, Ł.; Stefaniuk, I.; Wal, A.; Żywczak, A.; Dziejczak, A.; Maziarz, W. Magnetic and structural phase transition in  $\text{Ni}_{50}\text{Mn}_{35.5}\text{In}_{14.5}$  ribbon. *J. Magn. Magn. Mater.* **2019**, *485*, 21–26. [[CrossRef](#)]
7. González-Legarreta, L.; González-Alonso, D.; Rosa, W.O.; Caballero-Flores, R.; Suñol, J.J.; González, J.; Hernando, B. Magnetostructural phase transition in off-stoichiometric Ni-Mn-In Heusler alloy ribbons with low In content. *J. Magn. Magn. Mater.* **2015**, *383*, 190–195. [[CrossRef](#)]
8. Czaja, P.; Przewoźnik, J.; Hawelek, L.; Chrobak, A.; Zackiewicz, P.; Maziarz, W. Martensitic transformation, magnetic entropy, and adiabatic temperature changes in bulk and ribbon  $\text{Ni}_{48}\text{Mn}_{39.5}\text{Sn}_{12.5-x}\text{In}_x$  (x = 2, 4, 6) metamagnetic shape memory alloys. *J. Mater. Res.* **2021**, *36*, 3317–3328. [[CrossRef](#)]
9. Cejpek, P.; Proschek, P.; Straka, L.; Heczko, O. Dependence of martensitic transformation temperature on magnetic field in  $\text{Ni}_2\text{MnGa}$  and  $\text{Ni}_2\text{MnGa}_{0.95}\text{In}_{0.05}$  single crystals. *J. Alloys Compd.* **2022**, *908*, 164514. [[CrossRef](#)]
10. Liao, X.; Gao, L.; Wang, Y.; Xu, X.; Khan, M.T.; Chang, T.; Chen, K.; Zeng, Y.-J.; Yang, S.; Svedlindh, P. Large exchange bias in magnetic shape memory alloys by tuning magnetic ground state and magnetic-field history. *Sci. China Mater.* **2020**, *63*, 1291–1299. [[CrossRef](#)]
11. Yang, J.; Li, Z.; Yang, B.; Yan, H.; Cong, D.; Zhao, X.; Zuo, L. Effects of Co and Si co-doping on magnetostructural transformation and magnetocaloric effect in Ni-Mn-Sn based alloys. *J. Alloys Compd.* **2022**, *892*, 162190. [[CrossRef](#)]
12. Zhang, Y.; Li, S.; Hu, L.; Wang, X.; Li, L.; Yan, M. Excellent magnetocaloric performance in the carbide compounds  $\text{RE}_2\text{Cr}_2\text{C}_3$  (RE = Er, Ho, and Dy) and their composites. *Mater. Today Phys.* **2022**, *27*, 100786. [[CrossRef](#)]
13. Guo, D.; Moreno-Ramírez, L.M.; Law, J.Y.; Zhang, Y.; Franco, V. Excellent cryogenic magnetocaloric properties in heavy rare-earth based  $\text{HRENiGa}_2$  (HRE = Dy, Ho, or Er) compounds. *Sci. China Mater.* **2022**, 1–8. [[CrossRef](#)]

14. Rodionov, I.D.; Koshkid'ko, Y.S.; Cwik, J.; Quetz, A.; Pandey, S.; Aryal, A.; Dubenko, I.S.; Stadler, S.; Ali, N.; Titov, L.S.; et al. Magnetocaloric effect in Ni<sub>50</sub>Mn<sub>35</sub>In<sub>15</sub> Heusler alloy in low and high magnetic fields. *JETP Lett.* **2015**, *101*, 385–389. [[CrossRef](#)]
15. Umetsu, R.Y.; Ito, W.; Ito, K.; Koyama, K.; Fujita, A.; Oikawa, K.; Kanomata, T.; Kainuma, R.; Ishida, K. Anomaly in entropy change between parent and martensite phases in the Ni<sub>50</sub>Mn<sub>34</sub>In<sub>16</sub> Heusler alloy. *Scr. Mater.* **2009**, *60*, 25–28. [[CrossRef](#)]
16. Alves, R.F.; Correa, M.A.; Torquato, R.A.; dos Passos, T.A.; Bohn, F.; da Silva, R.B.; de Oliveira, D.F. Observation of quasi-diamagnetism and a transition from negative to positive in the exchange bias of a NiMnIn Heusler alloy. *J. Magn. Magn. Mater.* **2020**, *493*, 165691. [[CrossRef](#)]
17. Jing, C.; Chen, J.; Li, Z.; Qiao, Y.; Kang, B.; Cao, S.; Zhang, J. Exchange bias behavior and inverse magnetocaloric effect in Ni<sub>50</sub>Mn<sub>35</sub>In<sub>15</sub> Heusler alloy. *J. Alloys Compd.* **2009**, *475*, 1–4. [[CrossRef](#)]
18. Zhou, Z.N.; Yang, L.; Li, R.C.; Li, J.; Hu, Q.D.; Li, J.G. Martensitic transformations and kinetics in Ni-Mn-In-Mg shape memory alloys. *Intermetallics* **2018**, *92*, 49–54. [[CrossRef](#)]
19. Ma, T.Y.; Zhang, K.; Han, B.L.; Zhao, L.; Zhao, W.B.; Wang, C.; Liu, R.; Tian, X.H.; Tan, C.L. Simultaneous improvement on magnetic-field-induced working temperature and mechanical properties in Ni-Mn-In shape memory alloy. *AIP Adv.* **2022**, *12*, 065107. [[CrossRef](#)]
20. Liang, X.Z.; Bal, J.; Guang, Z.Q.; Zhang, Y.; Gu, J.L.; Zhang, Y.D.; Esling, C.; Zhao, X.; Zuo, L. Unravelong the phase stability and physical property of modulated martensite in Ni<sub>2</sub>Mn<sub>1.5</sub>In<sub>0.1</sub> alloy by first-principles calculations. *Materials* **2022**, *15*, 4032. [[CrossRef](#)] [[PubMed](#)]
21. Fang, M.X.; Tian, F.H.; Cao, Y.F.; Ke, X.Q.; Zhang, Y.; Yang, S.; Zuo, W.L.; Liu, Y.; Ma, T.Y.; Song, X.P. Understanding of the giant magnetic entropy change around the co-occurrence point of martensitic and magnetic transitions in Ni-Mn-In Heusler alloy. *Acta Mater.* **2022**, *229*, 117839. [[CrossRef](#)]
22. Ren, J.; Li, H.; Feng, S.; Zhai, Q.; Fu, J.; Luo, Z.; Zheng, H. Giant magnetocaloric effect in a Heusler Mn<sub>50</sub>Ni<sub>40</sub>In<sub>10</sub> unidirectional crystal. *Intermetallics* **2015**, *65*, 10–14. [[CrossRef](#)]
23. Bhohe, P.A.; Priolkar, K.R.; Nigam, A.K. Room temperature magnetocaloric effect in Ni–Mn–In. *Appl. Phys. Lett.* **2007**, *91*, 242503. [[CrossRef](#)]
24. Pathak, A.K.; Khan, M.; Gautam, B.R.; Stadler, S.; Dubenko, I.; Ali, N. Exchange bias in bulk Ni–Mn–In-based Heusler alloys. *J. Magn. Magn. Mater.* **2009**, *321*, 963–965. [[CrossRef](#)]
25. Sánchez-Llamazares, J.L.; Flores-Zuñiga, H.; Sánchez-Valdes, C.; Ross, C.A.; García, C. Refrigerant capacity of austenite in as-quenched and annealed Ni<sub>51.1</sub>Mn<sub>31.2</sub>In<sub>17.7</sub> melt spun ribbons. *J. Appl. Phys.* **2012**, *111*, 07A932. [[CrossRef](#)]
26. Zheng, H.X.; Wu, D.; Xue, S.; Frenzel, J.; Eggeler, G.; Zhai, Q. Martensitic transformation in rapidly solidified Heusler Ni<sub>49</sub>Mn<sub>39</sub>Sn<sub>12</sub> alloys. *Acta Mater.* **2012**, *59*, 5692–5699. [[CrossRef](#)]
27. Hernando, B.; Sánchez-Llamazares, J.L.; Santos, J.D.; Prida, V.M.; Baldomir, D.; Serantes, D.; Varga, R.; González, J. Magnetocaloric effect in melt spun Ni<sub>50.3</sub>Mn<sub>35.5</sub>Sn<sub>14.4</sub> ribbons. *Appl. Phys. Lett.* **2008**, *92*, 132507. [[CrossRef](#)]
28. Dadda, K.; Alleg, S.; Souilah, S.; Suñol, J.J.; Dhahri, E.; Bessais, L.; Hlil, E.K. Critical behavior, magnetic and magnetocaloric properties of melt-spun Ni<sub>50</sub>Mn<sub>35</sub>Sn<sub>15</sub> ribbons. *J. Alloys Compd.* **2018**, *735*, 1662–1672. [[CrossRef](#)]
29. Huang, K. *Statistical Mechanics*, 2nd ed.; Wiley: New York, NY, USA, 1987.
30. Lutterotti, L.; Matthies, S.; Wenk, H.R. MAUD: A friendly Java program for material analysis using diffraction. *News. CPD* **1999**, *21*, 14–15. Available online: <http://maud.radiographema.com> (accessed on 30 September 2021).
31. Çakır, A.; Acet, M.; Wiedwald, U.; Krenke, T.; Farle, M. Shell-ferromagnetic precipitation in martensitic off-stoichiometric Ni-Mn-In Heusler alloys produced by temper-annealing under magnetic field. *Acta Mater.* **2017**, *127*, 117–123. [[CrossRef](#)]
32. Yan, H.; Sánchez-Valdés, C.F.; Zhang, Y.; Llamazares, J.S.; Li, Z.; Yang, B.; Esling, C.; Zhao, X.; Zuo, L. Correlation between crystallographic and microstructural features and low hysteresis behavior in Ni<sub>50</sub>Mn<sub>35.25</sub>In<sub>14.75</sub> melt-spun ribbons. *J. Alloys Compd.* **2018**, *767*, 544–551. [[CrossRef](#)]
33. Cicek, M.M.; Saritas, S.; Yildirim, O.; Emre, B. Effect of the low constituent boron on martensitic transformation, magnetic, and magnetocaloric properties of Ni<sub>50</sub>Mn<sub>35</sub>In<sub>15</sub> Heusler alloys. *J. Alloys Compd.* **2020**, *845*, 155493. [[CrossRef](#)]
34. Banerjee, S.K. On a generalised approach to first and second order magnetic transitions. *Phys. Lett.* **1964**, *12*, 16–17. [[CrossRef](#)]
35. Stern-Taulats, E.; Castillo-Villa, P.O.; Mañosa, L.; Frontera, C.; Pramanick, S.; Majumdar, S.; Planes, A. Magnetocaloric effect in the low hysteresis Ni-Mn-In metamagnetic shape-memory Heusler Alloys. *J. Appl. Phys.* **2014**, *115*, 173907. [[CrossRef](#)]
36. Wederni, A.; Ipatov, M.; Pineda, E.; Suñol, J.J.; Escoda, L.; González, J.M.; Alleg, S.; Khitouni, M.; Zuberek, R.; Chumak, O.; et al. Magnetic properties, martensitic and magnetostructural transformations of ferromagnetic Ni–Mn–Sn–Cu shape memory alloys. *Appl. Phys. A* **2020**, *126*, 320. [[CrossRef](#)]
37. Arrott, A.; Noakes, J.E. Approximate Equation of State for Nickel Near its Critical Temperature. *Phys. Rev. Lett.* **1967**, *19*, 786–789. [[CrossRef](#)]
38. Nan, W.Z.; Thanh, T.D.; Nam, G.; You, T.S.; Piao, H.G.; Pan, L.Q.; Yu, S.C. Critical behavior near the ferromagnetic-paramagnetic transformation in the austenite phase of Ni<sub>43</sub>Mn<sub>46</sub>Sn<sub>8</sub>X<sub>3</sub> (X = In and Cr) Heusler alloys. *J. Magn. Magn. Mater.* **2017**, *443*, 171–178. [[CrossRef](#)]
39. Fisher, M.E.; Ma, S.K.; Nickel, B.G. Critical Exponents for Long-Range Interactions. *Phys. Rev. Lett.* **1972**, *29*, 917–920. [[CrossRef](#)]
40. Kouvel, J.S.; Fisher, M.E. Detailed Magnetic Behavior of Nickel Near its Curie Point. *Phys. Rev.* **1964**, *136*, 1626. [[CrossRef](#)]
41. Widom, B. Surface Tension and Molecular Correlations near the Critical Point. *J. Chem. Phys.* **1965**, *43*, 3892–3897. [[CrossRef](#)]



42. Zarai, E.; Issaoui, F.; Tozri, A.; Hussein, M.; Dhahri, E. Critical behavior near the paramagnetic to ferromagnetic phase transition temperature in  $\text{Sr}_{1.5}\text{Nd}_{0.5}\text{MnO}_4$  compound. *J. Supercond. Nov. Magn.* **2016**, *29*, 869–877. [[CrossRef](#)]
43. Zhang, L.; Fang, J.; Fan, J.; Ge, M.; Ling, L.; Zhang, C.; Zhang, Y. Critical behavior of the half-doped perovskite  $\text{Pr}_{0.5}\text{Sr}_{0.5}\text{CoO}_{3-\Delta}$ . *J. Alloys Compd.* **2014**, *588*, 294–299. [[CrossRef](#)]
44. Stanley, H.E. *Introduction to Phase Transitions and Critical Phenomena*; Oxford University Press: Oxford, UK, 1971.
45. Das, R.; Alagarsamy, P.; Srinivasan, A. Critical behavior and magnetic entropy change at magnetic phase transitions in  $\text{Ni}_{50}\text{Mn}_{35}\text{In}_{14}\text{Si}_1$  ferromagnetic shape memory Alloys. *Europhy. Lett.* **2014**, *108*, 66004.
46. Amaral, V.S.; Amaral, J.S. Magnetoelastic coupling influence on the magnetocaloric effect in ferromagnetic materials. *J. Magn. Mater.* **2004**, *272*, 2104–2105. [[CrossRef](#)]
47. Landau, L.D.; Lifschitz, E.M. *Statistical Physics Part 2. Course of Theoretical Physics*; Robert Maxwell, M.C., Ed.; P.I. Library: Oxford, NY, USA, 1958.